Multidimensional optical solitons and their manipulation in a cold atomic gas with a parity-time-symmetric optical Bessel potential

Lujia Jin [1], Chao Hang [1,2,3,*] and Guoxiang Huang[1,2,3]

[1]*State Key Laboratory of Precision Spectroscopy, East China Normal University, Shanghai 200062, China*
[2]*NYU-ECNU Joint Institute of Physics, New York University Shanghai, Shanghai 200062, China*
[3]*Collaborative Innovation Center of Extreme Optics, Shanxi University, Taiyuan, Shanxi 030006, China*

We propose a scheme to realize an optical Bessel potential with parity-time ($\mathcal{PT}$) symmetry and investigate the existence, propagation, and manipulation of multidimensional optical solitons through the interplay among diffraction, Kerr nonlinearity, and potential confinement in a cold atomic gas under the condition of electromagnetically induced transparency (EIT). We show that the system supports not only two-dimensional stationary optical solitons but also rotary ones; the stability of such solitons can be actively controlled by the gain-loss component (imaginary part), while the rotary motions can be tuned by the refractive-index component (real part) of the $\mathcal{PT}$-symmetric potential. Moreover, we demonstrate that the system allows the existence of stable three-dimensional spatiotemporal optical solitons, i.e., optical bullets, which have ultraslow propagation velocity and display helicoidal motions with controllable propagation trajectories. Due to the Kerr nonlinearity enhanced by the EIT effect, extremely low power is needed to create these multidimensional optical solitons. The results reported here are useful not only for the generation and manipulation of high-dimensional solitons via $\mathcal{PT}$-symmetric potentials, but also for promising applications in optical information processing and transmission.

I. INTRODUCTION

In the past decades, controls over nonlinear optical pulses and beams have attracted intense research interest due to their great importance not only in exploring the fundamental physics of nonlinear optical processes, but also in seeking practical applications of various nonlinear optical techniques [1,2]. Among various schemes suggested for manipulating optical solitons, the most important one is perhaps the use of spatial variations of optical medium properties (such as refractive index, gain, and loss) induced by modulated control laser fields. Based on such ideas, many types of optical solitons that do not exist in uniform nonlinear media have been discovered [3–5]. For example, in the presence of a radially modulated refractive index, fundamental, multipole, vortex, and annular solitons have been predicted theoretically [6–16] and observed experimentally [17,18]. In addition, a rich variety of stable two- and three-dimensional dissipative solitons (soliton complexes) and their motion have been studied in a spatially homogeneous medium with nonlinear gain and absorption [19,20].

On the other hand, to realize optical solitons without using intense laser field or long propagation distance, the resonant atomic gas working under the condition of electromagnetically induced transparency (EIT) [21] was proposed [22,23]. In such an optical medium, due to the quantum interference effect induced by a control laser field, the absorption of a probe laser field tuned to a strong one-photon resonance can be largely suppressed and hence the optical medium that is initially opaque becomes transparent; in particular, the Kerr nonlinearity of the system can be enhanced greatly. The optical solitons produced in such a system possesses many intriguing properties that are absent in conventional optical media. In particular, they generate very low power (order of 1 mW) and can form at very short propagation distance (order of 1 cm).

Another advantage of EIT-based atomic media lies in their efficiency in the *a priori* design of optical potentials by introducing modulations in the control laser field [24,25]. Since the optical potential in an EIT medium is usually complex, it can be designed in its real part and/or imaginary part, which stand for the refractive index and absorption (or gain) of the system, respectively. Based on such considerations, the construction of complex optical potentials with parity-time ($\mathcal{PT}$) symmetry [26,27] in atomic gases was proposed and realized in recent studies [28–33].

The system with a $\mathcal{PT}$-symmetric Hamiltonian has remarkable features. It can support all-real eigenvalues and allow a transition from a purely real spectrum to a complex one, referred to as $\mathcal{PT}$-symmetry breaking, which occurs at a critical depth of the imaginary part of the $\mathcal{PT}$-symmetric potential [5,34]. In optics, $\mathcal{PT}$-symmetry breaking manifests in a qualitative modification of light propagation and has many important applications [35–37]. Optical solitons were predicted in nonlinear optical media with various $\mathcal{PT}$-symmetric potentials [38–48]. Fundamental, dipole, and multipeak solitons were found to exist in nonlinear media with $\mathcal{PT}$-symmetric Bessel potentials [49–51]. However, most of these studies were limited to the case of one spatial dimension; the

_____
*Corresponding author: chang@phy.ecnu.edu.cn

investigation of multidimensional solitons and their active manipulation in the system with a two-dimensional (2D) $\mathcal{PT}$-symmetric Bessel potential is still absent; a practical system to realize the $\mathcal{PT}$-symmetric Bessel potential and soliton control is also needed.

In this work we propose a scheme to realize an optical Bessel potential with $\mathcal{PT}$ symmetry and explore the possibility of the existence, stable propagation, and active manipulation of multidimensional optical solitons in such a $\mathcal{PT}$-symmetric system. We consider a cold atomic gas working under the condition of EIT and show that the Bessel potential can be created through the transverse spatial modulation of the control field and an assistant field with an incoherent pumping. Due to the EIT effect, the system can possess giant Kerr nonlinearity and hence supports not only 2D [52] stationary optical solitons but also rotary ones. We also show that the stability of such solitons can be actively controlled by the gain-loss component (imaginary part), while the rotary motions can be tuned by the refractive-index component (real part) of the $\mathcal{PT}$-symmetric potential. Moreover, the existence of stable 2D spatial vortices is also predicted.

Furthermore, we demonstrate that the system allows stable 3D [52] spatiotemporal optical solitons (alias optical bullets), which have an ultraslow propagation velocity. Such multidimensional optical solitons can display helicoidal motions and their propagation trajectories can be controlled actively. Due to the giant Kerr nonlinearity in the system, to create these multidimensional optical solitons, only an extremely low power is required. The results reported in the present study are useful not only for the generation and manipulation of high-dimensional solitons via $\mathcal{PT}$-symmetric potentials but also for promising applications in optical information processing and transmission.

The remainder of the article is organized as follows. In Sec. II we describe the model under study and derive the nonlinear envelope equation. Section III discusses the physical realization of the $\mathcal{PT}$-symmetric Bessel potential and $\mathcal{PT}$-symmetry breaking in the system. Sections IV and V are devoted to our investigation of the existence, propagation, stability, and manipulation of 2D and 3D optical solitons, respectively. Section VI discusses the Doppler effect of the system. Section VII gives a summary of the main results obtained in this work.

II. MODEL AND NONLINEAR ENVELOPE EQUATION

A. Physical model

We start by considering a cold four-level atomic gas with an inverted-Y-type configuration, as shown in Fig. 1(a). A weak, spatially focused probe laser field $\mathbf{E}_p$ (with wave number $k_p = \omega_p/c$ and angular frequency ω_p) couples the atomic ground state $|1\rangle$ to the intermediate (excited) state $|3\rangle$, a strong control laser field $\mathbf{E}_c$ (with wave number $k_c = \omega_c/c$ and angular frequency ω_c) couples the low-lying state $|2\rangle$ to the state $|3\rangle$, and a strong assistant laser field $\mathbf{E}_a$ (with wave number $k_a = \omega_a/c$ and angular frequency ω_a) couples the state $|3\rangle$ to a high-lying state $|4\rangle$. Note that this excitation scheme combines a standard Λ-type EIT configuration (excitation channel $|1\rangle \leftrightarrow |3\rangle \leftrightarrow |2\rangle$) and a standard Ξ-type EIT
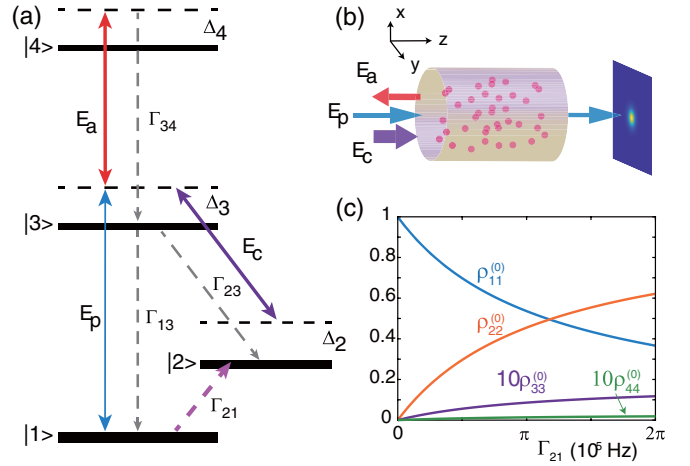

FIG. 1. (a) Level diagram and excitation scheme. A weak probe field $\mathbf{E}_p$, a strong control field $\mathbf{E}_c$, and a strong assistant field $\mathbf{E}_a$ couple the ground state $|1\rangle$ to the intermediate state $|3\rangle$, the low-lying state $|2\rangle$ to the state $|3\rangle$, and the intermediate state $|3\rangle$ to the high-lying state $|4\rangle$, respectively. Here Δ_j are detunings and Γ_{jl} are the spontaneous-emission decay rate from $|l\rangle$ to $|j\rangle$. An incoherent pumping (with pumping rate Γ_{21}) is used to pump atoms from $|1\rangle$ to $|2\rangle$, providing a gain to the probe field. The control and the assistant fields are assumed to be spatially modulated. (b) Possible geometric arrangement for the diffraction of the probe field when it is normally incident on the $\mathcal{PT}$-symmetric EIG. For details, see the text. (c) Populations $\rho_{\alpha\alpha}^{(0)}$ for the atoms at states $|\alpha\rangle$ ($\alpha = 1, 2, 3, 4$), as functions of the incoherent population pumping rate Γ_{21}.

configuration (excitation channel $|1\rangle \leftrightarrow |3\rangle \leftrightarrow |4\rangle$), providing abundant control parameters. The total electric field applied to the atomic gas is given by $\mathbf{E} = \mathbf{E}_p + \mathbf{E}_c + \mathbf{E}_a$, where $\mathbf{E}_\alpha = \mathbf{e}_\alpha \mathcal{E}_\alpha \exp[i(\mathbf{k}_\alpha \cdot \mathbf{r} - \omega_\alpha t)] + \text{c.c.}$, with $\mathbf{e}_\alpha$ the unit polarization vector and $\mathcal{E}_\alpha$ ($\alpha = p, c, a$) the field amplitude. The propagation direction of the probe field is assumed to be in the z direction, i.e., $\mathbf{k}_p = (0, 0, k_p)$. To eliminate the first-order Doppler effect, we set $\mathbf{k}_c = (0, 0, k_c)$ and $\mathbf{k}_a = (0, 0, -k_a)$, as shown in Fig. 1(b), in which the cylindrical domain is the atomic cell containing a gas of laser-cooled ^{87}Rb atoms (denoted by magenta circles).

In order to realize an optical $\mathcal{PT}$ symmetry in the present system, a gain mechanism of the probe field must be provided. To this end, we assume that an incoherent population pumping (with the pumping rate Γ_{21}) couples the ground state $|1\rangle$ and the low-lying state $|2\rangle$. Note that the incoherent population pumping can be implemented by using a couple of different techniques, such as intense atomic resonance spectrum lines emitted from hollow-cathode lamps or from microwave discharge lamps [53]. In addition, to create the required spatial distribution of the optical potential that satisfies the $\mathcal{PT}$ symmetry, the control and the assistant fields are assumed to have weak spatial modulations, which are easy to realize experimentally.

The dynamics of the system is described by the Hamiltonian $\hat{H} = \mathcal{N}_a \int d^3\mathbf{r}\, \hat{\mathcal{H}}(\mathbf{r}, t)$, with $\hat{\mathcal{H}}(\mathbf{r}, t)$ the Hamiltonian density and $\mathcal{N}_a$ the atom density. Under electric dipole and rotating-wave approximations, the Hamiltonian density in the interaction picture reads $\hat{\mathcal{H}}(\mathbf{r}, t) = \sum_{j=1}^{4} \hbar\Delta_j \hat{S}_{jj}(\mathbf{r}, t) - \hbar[\Omega_p \hat{S}_{13}(\mathbf{r}, t) + \Omega_a \hat{S}_{34}(\mathbf{r}, t) + \Omega_c \hat{S}_{23}(\mathbf{r}, t) + \text{H.c.}]$, where

$\hat{S}_{jl} = |l\rangle\langle j| e^{i[(\mathbf{k}_l - \mathbf{k}_j)\cdot\mathbf{r} - (\omega_l - \omega_j + \Delta_l - \Delta_j)t]}$ is the transition operator related to the states $|j\rangle$ and $|l\rangle$, satisfying the commutation relation $[\hat{S}_{jl}(\mathbf{r}, t), \hat{S}_{\mu\nu}(\mathbf{r}', t)] = (1/\mathcal{N}_a)\delta(\mathbf{r} - \mathbf{r}')[\delta_{j\nu}\hat{S}_{\mu l}(\mathbf{r}', t) - \delta_{\mu l}\hat{S}_{j\nu}(\mathbf{r}', t)]$. Here $\hbar\omega_j$ is the eigenenergy of the level $|j\rangle$; $\Delta_3 = \omega_p - (\omega_3 - \omega_1)$, $\Delta_2 = \omega_p - \omega_c - (\omega_2 - \omega_1)$, and $\Delta_4 = \omega_p + \omega_a - (\omega_4 - \omega_1)$ are frequency detunings; and $\Omega_p = (\mathbf{e}_p \cdot \mathbf{p}_{31})\mathcal{E}_p/\hbar$, $\Omega_c = (\mathbf{e}_c \cdot \mathbf{p}_{32})\mathcal{E}_c/\hbar$, and $\Omega_a = (\mathbf{e}_a \cdot \mathbf{p}_{43})\mathcal{E}_a/\hbar$ are Rabi frequencies of the probe, control, and assistant fields, respectively, with $\mathbf{p}_{ij}$ the electric dipole matrix elements associated with the transition $|i\rangle \leftrightarrow |j\rangle$. We assume that the high-lying state $|4\rangle$ is far-off-resonantly coupled to the intermediate state $|3\rangle$ through the assistant laser field $\mathbf{E}_a$, i.e., $|\Delta_3 - \Delta_4| \gg \Omega_a$, and hence the atomic population in the state $|4\rangle$ remains small during the evolution of the probe field.

The dynamics of the atomic motion is governed by the optical Bloch equation [54]

$$\frac{\partial\hat{\rho}}{\partial t} = -\frac{i}{\hbar}[\hat{H}, \hat{\rho}] - \Gamma[\hat{\rho}], \quad (1)$$

where ρ is density matrix and Γ is relaxation matrix, contributed from the spontaneous emission and dephasing of the atoms. Atomic density-matrix elements are defined by $\rho_{\alpha\beta} \equiv \langle\hat{S}_{\alpha\beta}\rangle$ ($\alpha, \beta = 1$–4), which describes the atomic population ($\alpha = \beta$) and atomic coherence ($\alpha \neq \beta$). The explicit form of Eq. (1) is presented in Appendix A. Under the slowly varying envelope approximation, the Maxwell equation for the probe field is reduced to

$$i\left(\frac{\partial}{\partial z} + \frac{1}{c}\frac{\partial}{\partial t}\right)\Omega_p + \frac{1}{2k_p}\nabla_\perp^2\Omega_p + \frac{k_p}{2}\chi_p\,\Omega_p = 0, \quad (2)$$

where $\nabla_\perp^2 = \partial_x^2 + \partial_y^2$ and $\chi_p = \mathcal{N}_\alpha(\mathbf{e}_p \cdot \mathbf{p}_{13})^2\rho_{31}/\varepsilon_0\hbar\Omega_p$ is the optical susceptibility of the probe field.

B. Two-dimensional nonlinear envelope equation and giant Kerr nonlinearity

Our main aim is to study the case where the probe field can be taken as a stationary nonlinear optical beam when it propagates in the system. The stationary state approximation is valid if the temporal duration τ_0 of the probe pulse is large enough so that $\tau_0 \gg \max(1/\Gamma_3, 1/\Gamma_4)$ (where Γ_α is the decay rate of the state $|\alpha\rangle$). Thus the evolution of the atomic population and coherence can adiabatically follow that of the probe field. Under such an assumption, the time-derivative terms in the Maxwell-Bloch (MB) equations (1) and (2) can be neglected, i.e., $\partial/\partial t = 0$, and thus the probe field behaves as a stationary optical beam.

Since the probe field is weak, the population in atomic levels changes little when the probe field is applied to the system and hence a perturbation expansion can be employed to solve the Bloch equation (1). Hence, we can employ the asymptotic expansions $\Omega_p = \epsilon\Omega_p^{(1)} + \epsilon^2\Omega_p^{(2)} + \cdots$ and $\rho_{\alpha\beta} = \rho_{\alpha\beta}^{(0)} + \epsilon\rho_{\alpha\beta}^{(1)} + \cdots$, where ϵ is the small parameter characterizing the typical amplitude of the probe field. By substituting the expansions into Eq. (1) and comparing the coefficients of ϵ^j ($j = 0, 1, \ldots$), we obtain a set of equations for $\rho_{\alpha\beta}^{(j)}$, which can be solved order by order.

The zeroth-order ($j = 0$) equations and their solutions describe the case when the probe field is not applied, i.e.,

$\Omega_p = 0$ (the details of these equations and their solutions are provided in Appendix B). A key parameter in the solution is the incoherent population pumping rate Γ_{21}. If $\Gamma_{21} = 0$, one has $\rho_{11}^{(0)} = 1$ with all other matrix elements being zero. In this case, all atoms are populated in the ground state $|1\rangle$ and hence the probe field will not acquire any gain when it is applied. However, if $\Gamma_{21} > 0$, one has $\rho_{33}^{(0)} > 0$, i.e., there are some atoms populated in the intermediate state $|3\rangle$, and hence the probe field will acquire gain due to the stimulated radiation effect, which is necessary for the realization of $\mathcal{PT}$ symmetry of the potential in the system. Since the condition $|\Delta_3 - \Delta_4|/\Omega_a \gg 1$ is satisfied in the system, the population in the high-lying state $|4\rangle$ is very small, i.e., $\rho_{44}^{(0)} \approx 0$. Figure 1(c) shows the population in each state $\rho_{\alpha\alpha}^{(0)}$ ($\alpha = 1$–4) as a function of Γ_{21}, where we have used the parameters of ^{87}Rb atoms given below. It can be seen that both $\rho_{22}^{(0)}$ and $\rho_{33}^{(0)}$ increase with the growth of Γ_{21}; however, $\rho_{44}^{(0)}$ remains nearly zero.

The linear evolution of the system is described by the solution of the first-order ($j = 1$) approximation. The solution of the probe field at this order reads $\Omega_p^{(1)} = F\exp\{i[K(\omega)z - \omega t]\}$, where F is an undetermined envelope function and $K(\omega)$ describes the linear dispersion relation

$$K(\omega) = \frac{\omega}{c} - \kappa_{13}\frac{(\omega + d_{21})(\omega + d_{41})}{D(\omega)}, \quad (3)$$

with $D(\omega) = (\omega + d_{21})(\omega + d_{31})(\omega + d_{41}) - |\Omega_a|^2(\omega + d_{21}) - |\Omega_c|^2(\omega + d_{41})$ and $\kappa_{13} = \mathcal{N}_a\omega_p|\mathbf{p}_{13}|^2/2\epsilon_0 c\hbar$. Here $d_{\alpha\beta} = \Delta_\alpha - \Delta_\beta + i\gamma_{\alpha\beta}$, with $\gamma_{\alpha\beta}$ the decay rate from $|\beta\rangle$ to $|\alpha\rangle$.

At the third-order ($j = 3$) approximation, we obtain a 2D [52] nonlinear Schrödinger (NLS) equation for Ω_p, given by

$$i\frac{\partial\Omega_p}{\partial z} + \frac{1}{2k_p}\nabla_\perp^2\Omega_p + \frac{k_p}{2}\left(\chi_p^{(1)} + \chi_p^{(3)}|\Omega_p|^2\right)\Omega_p = 0, \quad (4)$$

where

$$\chi_p^{(1)} = \frac{\mathcal{N}_\alpha(\mathbf{e}_p \cdot \mathbf{p}_{13})^2}{\varepsilon_0\hbar}\alpha_{31}^{(1)}, \quad (5)$$

$$\chi_p^{(3)} = \frac{\mathcal{N}_\alpha(\mathbf{e}_p \cdot \mathbf{p}_{13})^2}{\varepsilon_0\hbar D}\left[d_{21}d_{41}\left(\alpha_{33}^{(2)} - \alpha_{11}^{(2)}\right)\right.$$
$$\left. - d_{41}\Omega_c\alpha_{23}^{(2)} - d_{21}\Omega_a^*\alpha_{43}^{(2)}\right] \quad (6)$$

are the linear and third-order nonlinear optical susceptibilities, respectively. Explicit expressions of $\alpha_{31}^{(1)}$, $\alpha_{11}^{(2)}$, $\alpha_{33}^{(2)}$, $\alpha_{23}^{(2)}$, and $\alpha_{43}^{(2)}$ are given in Appendix B.

The physical model we considered above is rather general. One realistic system is a laser-cooled ^{87}Rb atomic gas, for which the atomic levels can be chosen as $|1\rangle = |5S_{1/2}, F = 1\rangle$, $|2\rangle = |5S_{1/2}, F = 2\rangle$, $|3\rangle = |5P_{3/2}\rangle$, and $|4\rangle = |6S_{1/2}\rangle$, with the decay rates $\Gamma_{13} \approx \Gamma_{23} \approx 2\pi \times 3$ MHz and $\Gamma_{34} \approx 2\pi \times 4$ kHz [55]. In addition, the incoherent population pumping rate $\Gamma_{21} \approx 2\pi \times 0.1$ MHz; the frequency detunings $\Delta_2 = 4.78 \times 10^6$ s^{-1}, $\Delta_3 = 1.2 \times 10^8$ s^{-1}, and $\Delta_4 = -1.5 \times 10^7$ s^{-1} (which give $|\Delta_3 - \Delta_4| \approx 1.35 \times 10^8$ s^{-1}); the atomic density $\mathcal{N}_a = 1.0 \times 10^{13}$ cm^{-3}; and the Rabi frequencies of the control and assistant fields are $\Omega_c = 3.0 \times 10^7$ s^{-1} and $\Omega_a = 4.5 \times 10^7$ s^{-1}. With these system parameters, we can

estimate the nonlinear optical susceptibility, given by

$$\chi_p^{(3)} \approx 5 \times 10^{-8} \text{ m}^2 \text{ V}^{-2}, \tag{7}$$

which is more than 10^{15} orders of magnitude larger than that obtained in conventional far-off-resonance nonlinear optical media (such as optical fibers) [54]. The reason is that the optical Kerr nonlinearity in the present system is greatly enhanced by the EIT effect.

In the above analysis, we have obtained the EIT-enhanced Kerr nonlinearity of the system by solving the MB equations adiabatically. However, the transient property of the Kerr nonlinearity is also important and relevant to most applications. In particular, the enhancement of the Kerr nonlinearity leads simultaneously to an increase in the settling time of the Kerr nonlinearity. In the present system, when the probe field is not applied (at the zeroth-order approximation), the coherence $\rho_{31} \approx 0$; when the probe field is applied (for the first-order approximation), ρ_{31} undergoes a damped oscillation and approaches its steady-state value $\rho_{31}^{(1)}(\infty) = \alpha_{31}^{(1)} \Omega_p$ (the expression of $\alpha_{31}^{(1)}$ is given in Appendix B). Since the probe susceptibility χ_p is proportional to ρ_{31}, the settling time of the Kerr nonlinearity (characterized by $\chi_p^{(3)}$) is determined by the transient behavior of ρ_{31}, which has the time-dependent solution [56]

$$\rho_{31}^{(1)} = \sum_{m=1}^{3} f_m e^{i\lambda_m t} + \rho_{31}^{(1)}(\infty), \tag{8}$$

where λ_m is the three eigenvalues of the matrix

$$M = \begin{pmatrix} d_{21} & \Omega_c^* & 0 \\ \Omega_c & d_{31} & \Omega_a^* \\ 0 & \Omega_a & d_{41} \end{pmatrix} \tag{9}$$

and f_m ($m = 1, 2, 3$) are slowly varying envelopes. Consequently, the settling time of the Kerr nonlinearity can be estimated by the reciprocal of the minimum of $\text{Im}(\lambda_m)$, i.e., $1/\min[\text{Im}(\lambda_m)]$, which is about 1.2 μs using the parameters given above Eq. (7).

For convenience in the following discussion, we write Eq. (4) in the dimensionless form

$$i\frac{\partial U}{\partial \zeta} + \left(\frac{\partial^2}{\partial \xi^2} + \frac{\partial^2}{\partial \eta^2} \right) U + V(\xi, \eta)U + W|U|^2 U = 0 \tag{10}$$

by defining the nondimensional variables $U = \Omega_p/U_0$, $\zeta = z/L_{\text{diff}}$, and $(\xi, \eta) = (x, y)/R_\perp$. Here U_0 and $R_\perp$ are the typical Rabi frequency and beam radius, respectively; $L_{\text{diff}} = 2k_p R_\perp^2 = 4\pi R_\perp^2/\lambda_p$ is the characteristic diffraction length of the probe field; and $V = k_p^2 R_\perp^2 \chi_p^{(1)}$ and $W = k_p^2 R_\perp^2 U_0^2 \chi_p^{(3)}$ are the dimensionless linear optical potential and nonlinearity coefficient, respectively. With the parameters of the ^{87}Rb atoms given above, we have $L_{\text{diff}} \approx 0.13$ cm and $W \approx 1$ if taking $U_0 \approx 1.5 \times 10^7$ s^{-1}.

III. $\mathcal{PT}$-SYMMETRIC BESSEL POTENTIAL AND $\mathcal{PT}$-SYMMETRY BREAKING

A. Realization of $\mathcal{PT}$-symmetric optical Bessel potential

Since the present system is highly configurable and manipulable, it is possible to create optical potentials with specific
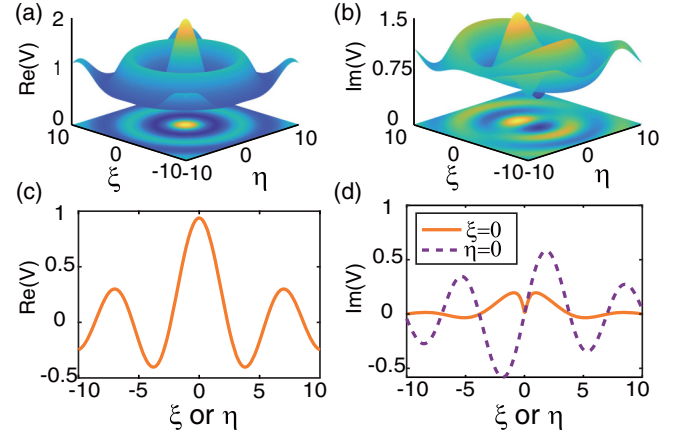

FIG. 2. Spatial distribution of the $\mathcal{PT}$-symmetric Bessel potential $V(\xi, \eta)$ (11) with $(V_0, V_1, V_2) = (0, 1, 1)$. (a) Surface plot of the real part $\text{Re}(V)$ of $V(\xi, \eta)$ as a function of ξ and η. (c) Profile of $\text{Re}(V)$ (as a function of ξ or η). (b) and (d) Same as (a) and (c), respectively, but for the imaginary part $\text{Im}(V)$. The profile of $\text{Im}(V)$ is an even function in the cross section $\xi = 0$ (yellow solid line) and an odd function in the cross section $\eta = 0$ (purple dashed line).

space distributions by modulating the control and assistant laser fields in space. As an example, the target potential can be designed to be in the form

$$V(\xi, \eta) = V_0 + V_1 J_0(\rho) + iV_2 J_1(\rho) \sin\theta, \tag{11}$$

where V_0 is a constant; V_1 and V_2 ($|V_1|, |V_2| \ll V_0$) characterize the amplitudes of the real part and the imaginary part, respectively; J_j is the jth-order Bessel function ($j = 0, 1$); and $\rho \equiv \sqrt{\xi^2 + \eta^2}$ and $\theta \equiv \arcsin(\eta/\rho)$ are the radial and angular coordinates, respectively. Figures 2(a) and 2(b) show surface plots of the real part $\text{Re}(V)$ and the imaginary part $\text{Im}(V)$ of $V(\xi, \eta)$, respectively, as functions of ξ and η with $(V_0, V_1, V_2) = (0, 1, 1)$; Figs. 2(c) and 2(d) show profiles of $\text{Re}(V)$ and $\text{Im}(V)$, respectively, as functions of ξ or η. We see that the imaginary part of the potential $V(\xi, \eta)$ is an even function in the ξ direction and an odd function in the η direction, i.e., $\text{Im}V(\xi, \eta) = \text{Im}V(-\xi, \eta)$ and $\text{Im}V(\xi, \eta) = -\text{Im}V(\xi, -\eta)$, which means that the target potential given by (11) satisfies the $\mathcal{PT}$ symmetry condition in two dimensions, i.e., $V(\xi, \eta)^* = V(-\xi, -\eta)^*$.

With the systemic parameters of ^{87}Rb atoms given above, the target potential (11) can be created using the method proposed in [28,31,33] by using the spatially modulated control and assistant fields of the form

$$\Omega_c(\xi, \eta)/\Omega_{c0} \approx 1 + 10^{-2} \times [0.56V_1 J_0(r)$$
$$+ 2.13V_2 J_1(r)\sin(\theta)], \tag{12a}$$

$$\Omega_a(\xi, \eta)/\Omega_{a0} \approx 1 + 10^{-2} \times [0.82V_1 J_0(r)$$
$$+ 4.38V_2 J_1(r)\sin(\theta)], \tag{12b}$$

with $\Omega_{c0} = 3.0 \times 10^7$ s^{-1} and $\Omega_{a0} = 4.5 \times 10^7$ s^{-1}. From Eq. (12) we see that the $\mathcal{PT}$-symmetric Bessel potential can be achieved by superposing zeroth- and first-order Bessel beams on the spatially uniform background of the control and assistant fields. Note that Bessel beams of different orders can be easily generated experimentally by illuminating a narrow
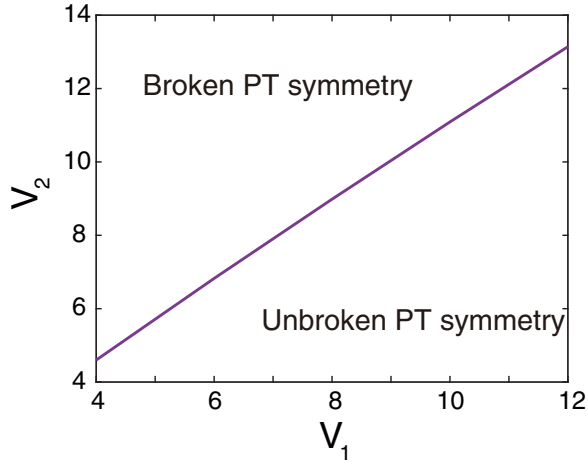
FIG. 3. Domains of unbroken (lower part) and broken (upper part) $\mathcal{PT}$-symmetry phases in the parameter plane of V_1 and V_2. The purple solid line gives the value of (V_1, V_2) where the $\mathcal{PT}$-symmetry breaking (phase transition) occurs.

annular split placed in the focal plane of a lens or axicon [57] or by using holographic techniques [58]; moreover, the diffraction-free property [59] of the Bessel beams can make the spatial modulations of the control and assistant fields very robust.

In fact, the control and assistant fields are not extended infinitely in space and both of them decay rapidly at their boundaries. Thereby, the uniform background and the Bessel beams will not lead to an infinitely high power. However, the waist of the probe beam is much smaller than that of the control and assistant beams and is highly focused in their center regions. Consequently, the intensity decay at boundaries of the control and assistant beams has only a marginal effect on the probe beam propagation and it is still subjected to the Bessel potential.

B. Linear-wave propagation and the breaking of $\mathcal{PT}$ symmetry

The stationary-state solutions of Eq. (10) with the $\mathcal{PT}$-symmetric optical Bessel potential (11) can be sought by assuming $U(\xi, \eta, \zeta) = u(\xi, \eta)e^{i\mu\zeta}$, where $u(\xi, \eta)$ is a mode function satisfying the equation

$$\mu u = \left(\frac{\partial^2}{\partial \xi^2} + \frac{\partial^2}{\partial \eta^2} \right)u + V(\xi, \eta)u + W|u|^2 u, \qquad (13)$$

with μ a propagation constant. If the probe field is very weak so that the nonlinear term $W|u|^2 u$ can be neglected, Eq. (13) is reduced to the linear eigenvalue problem $\mu u = (\partial_\xi^2 + \partial_\eta^2)u + V(\xi, \eta)u$, which describes the linear propagation of the probe field. When all eigenvalues μ are all real, the probe-field propagation is stable; however, if at least there is one eigenvalue that becomes complex, the probe-field propagation will be unstable. In fact, by tuning the amplitudes of the real and imaginary parts of V, i.e., V_1 and V_2, the eigenvalue μ can undergo a change from all real to partially complex and hence a phase transition from unbroken to broken $\mathcal{PT}$ symmetries occurs in the system.
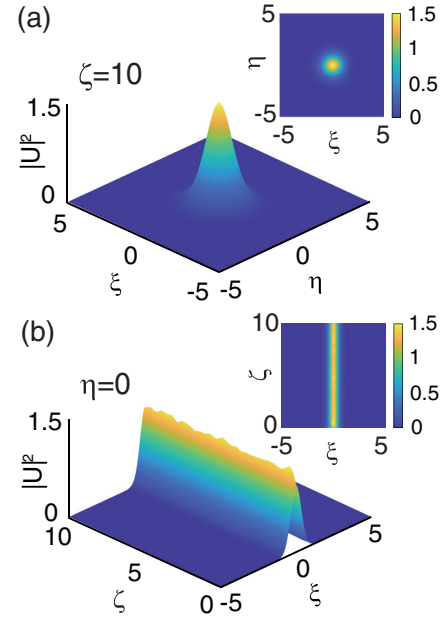

FIG. 4. A 2D stationary soliton in the presence of the $\mathcal{PT}$-symmetric Bessel potential (11) with $(V_1, V_2) = (4, 0.4)$. (a) Surface plot of the soliton intensity distribution $|U|^2 = |\Omega_p/U_0|^2$ as a function of $\xi = x/R_\perp$ and $\eta = y/R_\perp$ at $\zeta = z/L_{\text{diff}} = 10$ (i.e., $z = 10L_{\text{diff}} \approx 1.3$ cm). (b) Same as in (a) but shown as a function of $\xi = x/R_\perp$ and $\zeta = z/L_{\text{diff}}$ at $\eta = 0$. The insets in (a) and (b) show the corresponding top views of the soliton intensity distribution.

Figure 3 shows domains of the unbroken (lower part) and broken (upper part) $\mathcal{PT}$-symmetry phases in the parameter plane of V_1 and V_2. Remarkably, the boundary between the two domains is a straight line, denoted by the purple solid line in the figure, which can be fitted by the relation

$$V_2 \approx 1.05V_1 + 0.4. \qquad (14)$$

Each point on this line gives a set of values of (V_1, V_2), at which the $\mathcal{PT}$-symmetry breaking (phase transition) occurs. If $V_2 < 1.05V_1 + 0.4$, the system works in the phase of unbroken $\mathcal{PT}$ symmetry where the eigenvalue μ is real and thus the probe-field propagation is stable; however, if $V_2 > 1.05V_1 + 0.4$, the system works in the phase of broken $\mathcal{PT}$ symmetry where μ becomes complex and hence the probe-field propagation is unstable. From these results, we see that, by changing the control and assistant fields (12), it is possible to control the exceptional line (14) and the linear propagation of the probe field in the system.

IV. TWO-DIMENSIONAL SPATIAL SOLITONS UNDER THE $\mathcal{PT}$-SYMMETRIC BESSEL POTENTIAL

A. Stationary 2D optical solitons and vortices under the $\mathcal{PT}$-symmetric Bessel potential

Now we investigate the nonlinear propagation of the probe field based on the 2D NLS equation (10). By using numerical simulations, we find that Eq. (10) indeed supports stable 2D soliton solutions when the $\mathcal{PT}$-symmetric Bessel potential (11) is present. Figure 4(a) shows the intensity distribution $|U|^2 = |\Omega_p/U_0|^2$ for a 2D soliton as a function of $\xi = x/R_\perp$
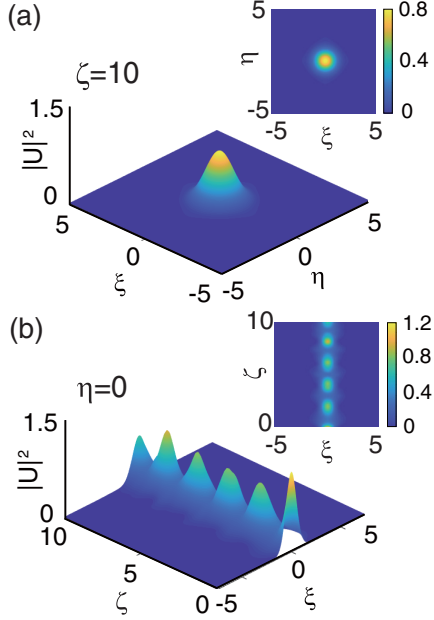
FIG. 5. Linear beam in the presence of the $\mathcal{PT}$-symmetric Bessel potential (11) with $(V_1, V_2) = (4, 0.4)$ without including Kerr nonlinearity. (a) Surface plot of the beam intensity distribution $|U|^2 = |\Omega_p/U_0|^2$ as a function of $\xi = x/R_\perp$ and $\eta = y/R_\perp$ at $\zeta = z/L_{\text{diff}} = 10$ (i.e., $z = 10L_{\text{diff}} \approx 1.3$ cm). (b) Same as in (a) but shown as a function of $\xi = x/R_\perp$ and $\zeta = z/L_{\text{diff}}$ at $\eta = 0$. The insets in (a) and (b) show the corresponding top views of the beam intensity distribution.

and $\eta = y/R_\perp$ at $\zeta = z/L_{\text{diff}} = 10$, i.e., $z = 10L_{\text{diff}} \approx 1.3$ cm. Amplitudes of the real and imaginary parts of the Bessel potential are taken to be $V_1 = 4$ and $V_2 = 0.4$, respectively. The initial condition used is a 2D Gaussian beam, i.e.,

$$U(\xi, \eta, \zeta = 0) = Ae^{-(\xi^2 + \eta^2)/w^2}, \quad (15)$$

where A and w are the beam amplitude and radius, respectively. In Fig. 4(c) we show $|U|^2$ as a function of $\xi = x/R_\perp$ and $\zeta = z/L_{\text{diff}}$ at $\eta = 0$ for $A = 1.2$ and $w = 1$. It can be seen that the intensity and width of the soliton remain nearly invariant, which indicates that the soliton is rather stable during propagation. Figures 4(b) and 4(d) are top views of the results given in Figs. 4(a) and 4(c), respectively.

The formation of the 2D soliton shown in Fig. 4 is due to the combined contribution from the diffraction, the $\mathcal{PT}$-symmetric Bessel potential (11), and the Kerr nonlinearity in the system. To demonstrate this, as a comparison in Fig. 5 we present a numerical result of the probe beam propagation in the linear case. In particular, when the typical Rabi frequency U_0 is decreased by one order, i.e., $U_0 = 1.5 \times 10^5$ s^{-1}, the nonlinear term of Eq. (10) is estimated as $W|U|^2 \sim 0.01$ with $W = 1$ and hence it can be safely neglected. Shown in Fig. 5(a) is the intensity distribution $|U|^2 = |\Omega_p/U_0|^2$ for a 2D optical beam in the linear case as a function of $\xi = x/R_\perp$ and $\eta = y/R_\perp$ at $\zeta = z/L_{\text{diff}} = 10$. The Bessel potential and initial condition adopted here are the same as those used in Fig. 4. It can be seen that in the absence of nonlinearity the maximum intensity of the probe beam is much smaller than that of the soliton (decreased by nearly
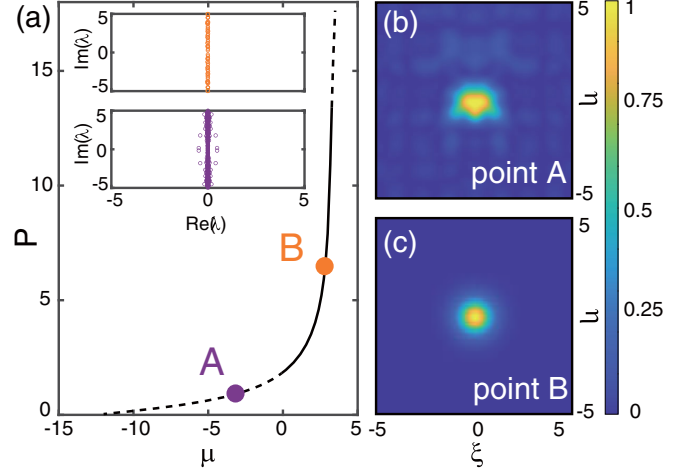

FIG. 6. Stability analysis of the 2D soliton. (a) Probe-field power $P = \iint |U|^2 d\xi \, d\eta$ as a function of the propagation constant μ for the $\mathcal{PT}$-symmetric Bessel potential (11) with $(V_1, V_2) = (4, 2)$. The solid part (where point A is located) and dashed part (where point B is located) of the curve represent stable and unstable regions of the soliton, respectively. The inserts show the stability spectra $\text{Re}(\lambda)$ and $\text{Im}(\lambda)$ (λ is the eigenvalue of the perturbations to the soliton) for small perturbations around the soliton for $P \approx 6.5$ (top panel) and $P \approx 1$ (bottom panel). Also shown are the top views of the soliton intensity distribution $|U|^2$ as a function of $\xi = x/R_\perp$ and $\eta = y/R_\perp$ for (b) $P \approx 6.5$ (corresponding to point A, where the soliton is stable) and (c) $P \approx 1$ (corresponding to point B, where the soliton is unstable).

50%). Moreover, an obvious oscillation of the beam intensity occurs during the propagation.

In order to have a strict analysis of the stability of the soliton, a linear stability analysis is performed, which is done by taking

$$U(\zeta, \xi, \eta) = e^{i\mu\zeta}[u_s(\xi, \eta) + p(\xi, \eta)e^{\lambda\zeta} + q^*(\xi, \eta)e^{\lambda^*\zeta}]. \quad (16)$$

Here $u_s(\xi, \eta)$ represents the soliton solution obtained numerically, μ is a propagation constant, p and q are small perturbations to the soliton, and λ is the eigenvalue of the perturbations. Based on Eq. (10), the eigenvalue problem for the perturbations is given by

$$-i\lambda p = [\mu + \partial_\xi^2 + \partial_\eta^2 + V(\xi, \eta) + 2W|u_s|^2]p + Wu_s^2 q, \quad (17a)$$

$$i\lambda q = [\mu + \partial_\xi^2 + \partial_\eta^2 + V^*(\xi, \eta) + 2W|u_s|^2]q + Wu_s^{*2}p. \quad (17b)$$

If at least one eigenvalue is found to have a positive real part, the soliton solution is unstable; otherwise they are stable.

The eigenvalue problem (17) is solved numerically by using the plane-wave expansion method [60]. Figure 6(a) shows the result of the probe-field power $P = \iint |U|^2 d\xi \, d\eta$ as a function of the propagation constant μ for the $\mathcal{PT}$-symmetric Bessel potential (11) with $(V_1, V_2) = (4, 2)$. The solid part (where point A is located) and the dashed part (where point B is located) of the curve of the figure represent stable and unstable regions of the soliton, respectively. Insets give
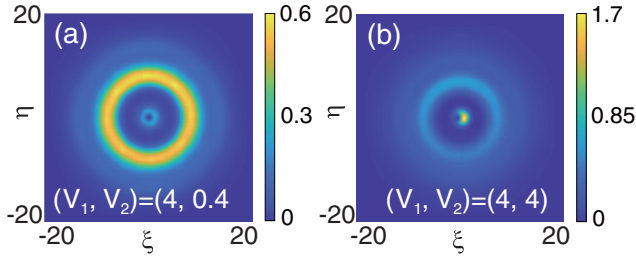
FIG. 7. The 2D vortex soliton solutions in the presence of the $\mathcal{PT}$-symmetric Bessel potential (11). (a) Top view of the intensity distribution $|U|^2 = |\Omega_p/U_0|^2$ of the stable vortex soliton as a function of $\xi = x/R_\perp$ and $\eta = y/R_\perp$ for $(V_1, V_2) = (4, 0.4)$. (b) Same as in (a) but for the unstable vortex soliton, obtained by taking $(V_1, V_2) = (4, 4)$.

stability spectra, i.e., the real part Re(λ) and imaginary part Im(λ) of the eigenvalue λ, for the perturbations around the soliton for $P \approx 6.5$ (top panel) and $P \approx 1$ (bottom panel). We find the following. (i) The soliton solution is stable in the interval $-3.2 \lesssim \mu \lesssim 0$ (denoted by the solid line), where $\partial P/\partial \mu < 0$. This agrees with the Vakhitov-Kolokolov (VK) criterion, which states that a fundamental soliton solution is stable if $\partial P/\partial \mu < 0$. (ii) The soliton becomes unstable when $\mu \lesssim -3.2$ and $\mu \gtrsim 0$ (denoted by the dashed line), where $\partial P/\partial \mu < 0$; this result is however contradicted by the VK criterion, which states that a fundamental soliton solution is unstable when $\partial P/\partial \mu > 0$. The reason that the VK criterion is not completely applicable in the present system is due to the existence of the gain and loss in the Bessel potential, which makes the VK criterion invalid. Figures 6(b) and 6(c) are top views of the soliton intensity distribution $|U|^2$ as a function of $\xi = x/R_\perp$ and $\eta = y/R_\perp$ for $P \approx 6.5$ (corresponding to point A, where the soliton is stable) and $P \approx 1$ (corresponding to point B, where the soliton is unstable).

Besides the fundamental soliton solution found above, the system supports also stable vortex solitons, which carry orbital angular momenta. To demonstrate this, we take the initial condition to be a 2D vortex beam

$$U(\xi, \eta, \zeta = 0) = A\left(\frac{\sqrt{2}\rho}{w}\right)^{|l|} e^{-\rho^2/w^2} L_p^{|l|}\left(\frac{2\rho^2}{w^2}\right) e^{il\varphi}, \quad (18)$$

where A and w are the amplitude and radius of the beam, respectively; $\rho = \sqrt{\xi^2 + \eta^2}$; $L_p^{|l|}$ is the generalized Laguerre-Gaussian (LG) polynomial, with l (p) the radial (azimuthal) index; and φ is the azimuthal angle. The orbital angular momentum of a vortex soliton is proportional to the topological charge or vorticity, determined by l.

Figure 7(a) shows the top view of the intensity distribution $|U|^2 = |\Omega_p/U_0|^2$ of a stable vortex soliton for $A = 0.77$ and $w = 2$ as a function of $\xi = x/R_\perp$ and $\eta = y/R_\perp$ in the presence of the $\mathcal{PT}$-symmetric Bessel potential (11) with $(V_1, V_2) = (4, 0.4)$. The LG polynomial of the initial condition (18) is taken as the lowest-order one, i.e., L_0^1; hence the topological charge of the vortex soliton is one. We see that the vortex soliton has no obvious deformation after propagating to $\zeta = z/L_{\text{diff}} = 10$, i.e., $z = 10L_{\text{diff}} \approx 1.3$ cm. However, such a vortex soliton loses its stability when decreasing

(increasing) the real-part (imaginary-part) amplitude of the potential V_1 (V_2). Figure 7(b) shows the result of an unstable vortex soliton, which is obtained by taking $(V_1, V_2) = (4, 4)$, i.e., V_2 is enlarged. Because $(V_1, V_2) = (4, 4)$ is located in the unbroken-$\mathcal{PT}$-symmetry phase (see Fig. 3), the instability of the vortex soliton is not stemmed from the $\mathcal{PT}$-symmetry breaking.

The imaginary part of the Bessel potential (11) can have a significant effect on the stability of the fundamental and vortex solitons. Specifically, when the system works in the broken-$\mathcal{PT}$-symmetry region, the solitons are unstable. However, when the system works in the unbroken-$\mathcal{PT}$-symmetry region but close to the phase transition points, i.e., the points on the purple line in Fig. 3, the solitons may still be unstable. The is because the Kerr nonlinearity can modify the linear potential and induce the symmetry breaking for a linear system with unbroken $\mathcal{PT}$ symmetry [61]. Thus, the solitons obtained here are stable only when the system works in the unbroken-$\mathcal{PT}$-symmetry region and far from the phase transition points.

B. Rotary 2D solitons

The fundamental solitons found above are confined nearly to the center of the Bessel potential (11), where the potential energy reaches its smallest value. We now demonstrate that solitons can also be initially set at and then rotate stably around an outer ring of the Bessel potential. The possibility of such a rotary soliton lies in the fact that the Bessel potential is minimum and degenerate in each outer ring. Hence, the soliton can move along the ring with the minimum potential energy if it is created initially at the ring with the transverse velocity being tangent to the ring.

In order to have deeper rings (thus stronger potential confinement), we can change the real part of the $\mathcal{PT}$-symmetric Bessel potential (11) from the zeroth-order Bessel function J_0 to the first-order Bessel function J_1, i.e.,

$$V(\xi, \eta) = V_0 + V_1 J_1(\rho) + iV_2 J_1(\rho) \sin\theta. \quad (19)$$

Figure 8 shows the result of numerical simulation on a rotary soliton located at the first ring of the $\mathcal{PT}$-symmetric Bessel potential (19) for $(V_1, V_2) = (12, 2)$. Figures 8(a), 8(b), 8(c), and 8(d) show the intensity distribution $|U|^2 = |\Omega_p/U_0|^2$ of the soliton as a function of $\xi = x/R_\perp$ and $\eta = y/R_\perp$ when $\zeta = z/L_{\text{diff}} = 0, 2, 4$, and 5, respectively. The initial condition used is a 2D Gaussian beam, i.e.,

$$U(\xi, \eta, \zeta = 0) = A\, e^{-[\xi^2 + (\eta - r_0)^2]/w^2 + iV_\perp \xi}, \quad (20)$$

where r_0 is the radius of the first ring and $V_\perp$ denotes the initial transverse velocity tangential to the ring. In the simulation, we have chosen $r_0 \approx 2$, $V_\perp \approx 0.8$, $A = 0.4$, and $w = 1$. We see that the soliton keeps its waveform nearly invariant during its rotation around the ring. However, when the initial transverse velocity exceeds a threshold value, i.e., $V_\perp > V_\perp^{\text{th}} \approx 2.4$, the soliton cannot be trapped in the first ring anymore and it will escape from the ring tangentially due to the high centrifugal force. Nevertheless, such escape behavior can be suppressed by increasing the amplitude of the real part of the Bessel potential, i.e., by enlarging V_1.

The maximum average power P_{max} to generate the stationary and rotary 2D solitons described above can be obtained by
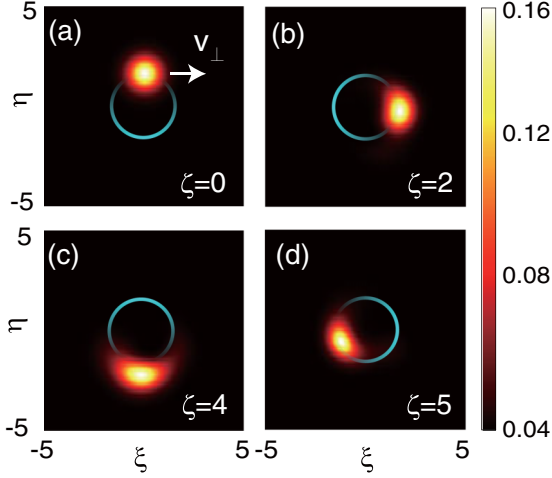
FIG. 8. The 2D rotary soliton located at the first ring of the $\mathcal{PT}$-symmetric Bessel potential (19) with $(V_1, V_2) = (12, 2)$. The radius of the first Bessel ring is $r_0 \approx 2$; the initial tangent velocity of the soliton is $V_\perp \approx 0.8$. The top views of the soliton intensity distribution $|U|^2 = |\Omega_p/U_0|^2$ are shown as functions of $\xi = x/R_\perp$ and $\eta = y/R_\perp$ for $\zeta = z/L_{\text{diff}}$ equal to (a) 0, (b) 2, (c) 4, and (d) 5.

using the Poynting vector [23], which is estimated to be

$$P_{\max} = 2\epsilon_0 c n_p S_0 |E_p|^2_{\max} \approx 2.07 \text{ nW}. \tag{21}$$

Thus, a very low generation power is needed to produce the stable 2D solitons in the present system as the optical Kerr nonlinearity is greatly enhanced by the EIT effect.

V. THREE-DIMENSIONAL SPATIOTEMPORAL SOLITONS UNDER THE $\mathcal{PT}$-SYMMETRIC BESSEL POTENTIAL

Finally, we turn to investigate the case where the stationary-state approximation of the probe field used above cannot be applied. If the temporal duration of the probe field is shortened, e.g., order of hundreds of nanoseconds, the dispersion effect will play a significant role and it must be taken into account for the evolution of the probe field. In this situation, the 2D NLS equation (4) is modified into the 3D one [52]

$$i\left(\frac{\partial}{\partial z} + \frac{1}{V_g}\frac{\partial}{\partial t}\right)\Omega_p - \frac{1}{2}K_2\frac{\partial^2 \Omega_p}{\partial t^2} + \frac{1}{2k_p}\nabla_\perp^2 \Omega_p$$
$$+ \frac{k_p}{2}\left(\chi_p^{(1)} + \chi_p^{(3)}|\Omega_p|^2\right)\Omega_p = 0, \tag{22}$$

where $V_g = (\partial K/\partial\omega)^{-1}$ is the group velocity of the probe field and $K_2 = \partial^2 K/\partial\omega^2$ is the parameter denoting group-velocity dispersion. Here $K(\omega)$ is the linear dispersion relation of the system, given by the expression (3).

The dimensionless form of Eq. (22) reads

$$i\frac{\partial U}{\partial\zeta} + \left(\frac{\partial^2}{\partial T^2} + \frac{\partial^2}{\partial\xi^2} + \frac{\partial^2}{\partial\eta^2}\right)U + V(\xi, \eta)U$$
$$+ W|U|^2 U = 0. \tag{23}$$

Here $T = (t - z/V_g)/\tau_0$ is a nondimensional (propagation) variable ($\tau_0 \equiv R_\perp\sqrt{k_p|K_2|}$ is the probe-pulse duration); the definitions of the other quantities in the equation are the same as those used in Eq. (10). Moreover, to obtain Eq. (23) we
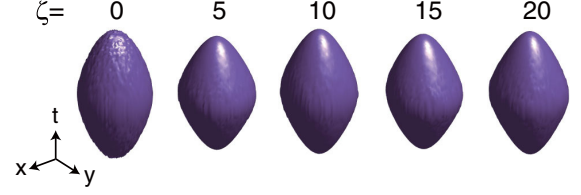

FIG. 9. Propagation of the optical bullet located at the center of the $\mathcal{PT}$-symmetric Bessel potential (11) for $(V_1, V_2) = (4, 0.2)$. Shown are isosurface plots of the optical bullet when propagating to distances $\zeta = z/L_{\text{diff}} = 0, 5, 10, 15, 20$ (i.e., $z = 0, 0.65, 1.3, 1.95, 2.6$ cm), respectively.

have also defined the characteristic dispersion length $L_{\text{disp}} = 2\tau_0^2/|K_2|$, which is set to equal to the characteristic diffraction length L_{diff}, i.e., $L_{\text{disp}} = L_{\text{diff}}$. Additionally, we have assumed that the (dispersion) coefficient of the term $\partial^2 U/\partial T^2$ is positive, which means that the group-velocity dispersion has been chosen to be negative, i.e., sgn(K_2) = −1.

Equation (23) supports the existence of 3D spatiotemporal solitons (also called optical bullets [1,2,62]), which are localized in three spatial dimensions and also in time. Figure 9 shows the result of numerical simulations on a typical optical bullet by assuming $\tau_0 = 0.13$ μs. It is located at the center of the $\mathcal{PT}$-symmetric Bessel potential (11) for $(V_1, V_2) = (4, 0.2)$. Illustrated in the figure is an isosurface plot of the intensity distribution $|U|^2$ of the optical bullet as a function of $\xi = x/R_\perp$, $\eta = y/R_\perp$, and $T = (t - z/V_g)/\tau_0$, when propagating to distances $\zeta = z/L_{\text{diff}} = 0, 5, 10, 15$, and 20, i.e., $z = 0, 0.65, 1.3, 1.95$, and 2.6 cm, respectively. The initial condition used in the simulation is a 3D Gaussian wave packet, i.e.,

$$U(\xi, \eta, T, \zeta = 0) = A\, e^{-(\xi^2+\eta^2)/w^2 - T^2/\tau_0^2}, \tag{24}$$

with $A = 1.2$ and $w = 1$. One sees that, after propagating to the distance $\zeta = z/L_{\text{diff}} = 5$, i.e., $z = 5L_{\text{diff}} \approx 0.65$ cm, the initial Gaussian wave packet is transformed to a waveform of a smooth optical bullet.

To test the stability of the optical bullet, we take $U = (1 + \epsilon f_R)u_{\text{OB}}$ and let it propagate in the system. Here u_{OB} is the optical bullet solution, ϵ is a parameter representing the typical amplitude of the perturbation to the bullet, and f_R is a random variable uniformly distributed in the interval [0, 1]. We observe that the optical bullet relaxes to the self-cleaned form close to the unperturbed one. This point can be seen clearly from the figure where the optical bullet undergoes no apparent change when it propagates to $\zeta = z/L_{\text{diff}} = 20$, i.e., $z = 20L_{\text{diff}} \approx 2.6$ cm. Therefore, the optical bullet obtained is quite stable during propagation.

If the optical bullet is initially created not at the center but at an outer ring of the potential (19), it will rotate helically around the ring. Figure 10 shows the helical motion of the optical bullet that is generated in the first ring of the potential (19) with $(V_1, V_2) = (12, 2)$. The solid (dashed) line in the figure denotes the propagation trajectory of the optical bullet for the initial transverse velocity taken to be $V_\perp = 0.46$ ($V_\perp = 0.23$). The isosurface plots of the optical bullet at $\tau = 0, 3$, and 6 (corresponding to $t \approx 0, 0.4$, and 0.8 μs, respectively) are illustrated by purple domains. The reason for the helical
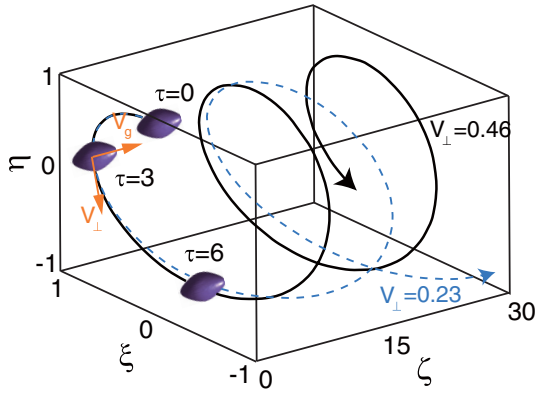
FIG. 10. Helical motion of the optical bullet created in the first ring of the potential (19) with $(V_1, V_2) = (12, 2)$. The solid (dashed) line denotes the propagation trajectory of the optical bullet for initial transverse velocity $V_\perp = 0.46$ ($V_\perp = 0.23$). Domains illustrated in purple are isosurface plots of the optical bullet at $\tau = 0, 3$, and 6, respectively.

motion of the optical bullet is that the velocity of the optical bullet has two orthogonal components, i.e., the group velocity V_g (in the z direction) and the transverse velocity $V_\perp$ (in the x direction).

The group velocity of the probe pulse can be estimated using the system parameters given above, which reads

$$V_g \approx 1.7 \times 10^{-4} c, \tag{25}$$

which is much slower than c (the light speed in vacuum). For the optical bullet located at the center of the $\mathcal{PT}$-symmetric Bessel potential (Fig. 9), its propagating velocity is equal to V_g, which means that the optical bullet obtained in the present system has an ultraslow propagation velocity in comparison with the light speed in vacuum. For the optical bullet that displays the helical motion (Fig. 10), its propagation velocity is also ultraslow because the transverse velocity component $V_\perp$ is at the same order of V_g. Note that, due to the controllability of the system, we can actively manipulate the helical trajectory and hence the output position of the optical bullet by changing either V_g or $V_\perp$. For instance, by reducing $V_\perp$ to half its value, the rotation number of the optical bullet will be decreased by half for the same propagation distance. By using the Poynting vector, the maximum average power $P_{\max}$ to generate the optical bullet described above can be estimated to be

$$P_{\max} \approx 5.18 \text{ nW}, \tag{26}$$

which is very low due to the EIT-enhanced optical Kerr nonlinearity.

VI. DISCUSSION

Here we briefly discuss the Doppler effect due to the thermal motion of the atoms. With the given propagation directions of the probe, control, and assistant laser fields (see the first paragraph of Sec. II A), our results can be readily generalized when an atom moves with a velocity $\mathbf{V}$ by the replacement $\Delta_3 \rightarrow \omega_p - (\omega_3 - \omega_1) + k_p V_z$, $\Delta_2 \rightarrow \omega_p - \omega_c - (\omega_2 - \omega_1) + (k_p - k_c) V_z$, and $\Delta_4 \rightarrow \omega_p + \omega_a - (\omega_4 - \omega_1) +$

$(k_p + k_a) V_z$, with V_z the projection of $\mathbf{V}$ in the z direction. For a thermal atomic gas, the V_z-dependent terms should be averaged over the Maxwell velocity distribution $f(V_z) = 1/(\sqrt{\pi} V_T) e^{-(V_z/V_T)^2}$, where $V_T = (2k_B T/M)^{1/2}$ is the most probable speed, with k_B the Boltzmann constant, T the atomic temperature, and M the atomic mass. With these expressions we see that the velocity-dependent effect in the two-photon detunings, i.e., Δ_2 and Δ_4, can be largely eliminated when the probe and control fields copropagate and the probe and assistant fields counterpropagate in the z direction, respectively. Consequently, the Doppler effect in the two-photon detunings, i.e., the first-order Doppler effect, can usually be neglected compared with that in the one-photon detuning, Δ_3.

In order to find applications of our system in optical information processing, it is crucial to have a high-accuracy $\mathcal{PT}$ symmetry of the Bessel potential, which can be realized by lowing the temperature of the atomic gas so that the Doppler effect in the one-photon detuning Δ_3 can be neglected. The latter condition is satisfied when $\omega_p - (\omega_3 - \omega_1) \gg k_p V_z \sim k_p V_T$, which results in $T \ll 1.2$ K with the given parameters. Thus, the temperature of the atomic gas should be lowered to 0.1 K at least to obtain a high-accuracy $\mathcal{PT}$ symmetry. Moreover, since the length of the atomic medium reads $L = 1.3$ cm, the processing time of optical information is about $L/c \approx 43$ ps.

VII. CONCLUSION

To sum up, we have proposed a physical scheme to realize a Bessel potential with $\mathcal{PT}$ symmetry in a laser-driven cold atomic gas under the condition of EIT. The existence, propagation, and manipulation of 2D and 3D optical solitons are investigated through the interplay among diffraction, potential confinement, and Kerr nonlinearity of the system. We have shown that the system supports 2D stationary and rotary spatial solitons; their stability property is significantly dependent on the gain-loss component (imaginary part) of the Bessel potential, while their motion can be controlled by the real part of the potential. Moreover, the system also supports stable 2D spatial vortices. We have demonstrated that the system allows stable 3D spatiotemporal solitons (light bullets), which have ultraslow propagation velocity and can perform helicoidal motion with a controllable trajectory in 3D space. Due to the EIT-enhanced Kerr nonlinearity in the system, all multidimensional solitons found here require only very low generation power. The results reported are not only useful for providing a new route for generating and manipulating multidimensional optical solitons, but also promising for potential applications in optical information processing and transmission.

APPENDIX A: OPTICAL BLOCH EQUATION

Based on the Hamiltonian $\hat{H}$ given in the main text, we can obtain the explicit expression of the optical Bloch equation

$$i\left(\frac{\partial}{\partial t} + \Gamma_{21}\right)\rho_{11} - i\Gamma_{13}\rho_{33} - \Omega_p\rho_{13} + \Omega_p^*\rho_{31} = 0, \quad \text{(A1a)}$$

$$i\frac{\partial}{\partial t}\rho_{22} - i\Gamma_{21}\rho_{11} - i\Gamma_{23}\rho_{33} - \Omega_c\rho_{23} + \Omega_c^*\rho_{32} = 0, \quad \text{(A1b)}$$

$$i\left(\frac{\partial}{\partial t} + \Gamma_3\right)\rho_{33} - i\Gamma_{34}\rho_{44} + \Omega_p\rho_{13} - \Omega_p^*\rho_{31} + \Omega_c\rho_{23}$$
$$- \Omega_c^*\rho_{32} - \Omega_a\rho_{34} + \Omega_a^*\rho_{43} = 0, \quad \text{(A1c)}$$

$$i\frac{\partial}{\partial t}\rho_{44} + i\Gamma_{34}\rho_{44} + \Omega_a\rho_{34} - \Omega_a^*\rho_{43} = 0 \quad \text{(A1d)}$$

for the diagonal elements and

$$\left(i\frac{\partial}{\partial t} + d_{21}\right)\rho_{21} + \Omega_c^*\rho_{31} - \Omega_p\rho_{23} = 0, \quad \text{(A2a)}$$

$$\left(i\frac{\partial}{\partial t} + d_{31}\right)\rho_{31} + \Omega_p(\rho_{11} - \rho_{33}) + \Omega_c\rho_{21} + \Omega_a^*\rho_{41} = 0, \quad \text{(A2b)}$$

$$\left(i\frac{\partial}{\partial t} + d_{41}\right)\rho_{41} + \Omega_a\rho_{31} - \Omega_p\rho_{43} = 0, \quad \text{(A2c)}$$

$$\left(i\frac{\partial}{\partial t} + d_{32}\right)\rho_{32} + \Omega_p\rho_{12} + \Omega_c(\rho_{22} - \rho_{33}) + \Omega_a^*\rho_{42} = 0, \quad \text{(A2d)}$$

$$\left(i\frac{\partial}{\partial t} + d_{42}\right)\rho_{41} + \Omega_a\rho_{32} - \Omega_c\rho_{43} = 0, \quad \text{(A2e)}$$

$$\left(i\frac{\partial}{\partial t} + d_{43}\right)\rho_{43} + \Omega_a(\rho_{33} - \rho_{44}) - \Omega_p^*\rho_{41} - \Omega_c^*\rho_{42} = 0 \quad \text{(A2f)}$$

for the nondiagonal elements. Here $\rho_{\alpha\beta} \equiv \langle\hat{S}_{\alpha\beta}\rangle = \langle\Psi_0|\hat{S}_{\alpha\beta}|\Psi_0\rangle$ ($|\Psi_0\rangle$ is the initial state vector of the system), $d_{ij} = \Delta_i - \Delta_j + i\gamma_{ij}$, $\gamma_{ij} = (\Gamma_i + \Gamma_j)/2 + \gamma_{ij}^{\text{col}}$ ($i \neq j$), and $\Gamma_j = \sum_{i<j}\Gamma_{ij}$, with Γ_{ij} the spontaneous emission decay rate and γ_{ij}^{col} the dephasing rate from $|j\rangle$ to $|i\rangle$.

APPENDIX B: SOLUTIONS OF THE OPTICAL BLOCH EQUATION

By substituting the asymptotic expansions $\Omega_p = \epsilon\Omega_p^{(1)} + \epsilon^2\Omega_p^{(2)} + \cdots$ and $\rho_{jl} = \rho_{jl}^{(0)} + \epsilon\rho_{jl}^{(1)} + \cdots$ (ϵ is a small parameter characterizing the typical amplitude of the probe field) into Eq. (1) and comparing the coefficients of ϵ^m ($m = 0, 1, \ldots$), we obtain a set of equations for $\rho_{jl}^{(m)}$, which can be solved order by order. The zeroth-order equations are given by

$$\begin{pmatrix} -\Gamma_{21} & 0 & \Gamma_{13} \\ \Gamma_{21} & 0 & \Gamma_{23} \\ 1 & 1 & 1 \end{pmatrix}\begin{pmatrix} \rho_{11}^{(0)} \\ \rho_{22}^{(0)} \\ \rho_{33}^{(0)} \end{pmatrix} = \begin{pmatrix} 0 \\ 2\,\text{Im}(\Omega_c^*\rho_{32}^{(0)}) \\ 1 \end{pmatrix}. \quad \text{(B1)}$$

In order to solve $\rho_{32}^{(0)}$, we also need equations for $\rho_{32}^{(0)}$, $\rho_{42}^{(0)}$, and $\rho_{43}^{(0)}$, which are given by

$$\begin{pmatrix} d_{32} & \Omega_a^* & 0 \\ \Omega_a & d_{42} & -\Omega_c \\ 0 & -\Omega_c^* & d_{43} \end{pmatrix}\begin{pmatrix} \rho_{32}^{(0)} \\ \rho_{42}^{(0)} \\ \rho_{43}^{(0)} \end{pmatrix} = \begin{pmatrix} \Omega_c(\rho_{33}^{(0)} - \rho_{22}^{(0)}) \\ 0 \\ -\Omega_a\rho_{33}^{(0)} \end{pmatrix}. \quad \text{(B2)}$$

The solutions of Eqs. (B1) and (B2) read

$$\rho_{11}^{(0)} = -\Gamma_{13}X/[\Gamma_{21}\Gamma_{13} - (\Gamma_{21} + \Gamma_{13})X + \Gamma_{21}(\Gamma_{23} + Y)], \quad \text{(B3a)}$$

$$\rho_{22}^{(0)} = \Gamma_{21}(\Gamma_{13} + \Gamma_{23} + Y)/[\Gamma_{21}\Gamma_{13} - (\Gamma_{21} + \Gamma_{13})X + \Gamma_{21}(\Gamma_{23} + Y)], \quad \text{(B3b)}$$

$$\rho_{33}^{(0)} = -\Gamma_{21}X/[\Gamma_{21}\Gamma_{13} - (\Gamma_{21} + \Gamma_{13})X + \Gamma_{21}(\Gamma_{23} + Y)], \quad \text{(B3c)}$$

$$\rho_{32}^{(0)} = [-(d_{42}d_{43} - |\Omega_c|^2)\rho_{22}^{(0)} + (d_{42}d_{43} - |\Omega_c|^2 + |\Omega_a|^2)\rho_{33}^{(0)}]\Omega_c/Z, \quad \text{(B3d)}$$

$$\rho_{42}^{(0)} = [d_{43}\rho_{22}^{(0)} - (d_{32} + d_{43})\rho_{33}^{(0)}]\Omega_c\Omega_a/Z, \quad \text{(B3e)}$$

$$\rho_{43}^{(0)} = [|\Omega_c|^2\rho_{22}^{(0)} - (d_{32}d_{42} + |\Omega_c|^2 - |\Omega_a|^2)\rho_{33}^{(0)}]\Omega_a/Z, \quad \text{(B3f)}$$

$$\rho_{21}^{(0)} = \rho_{31}^{(0)} = \rho_{41}^{(0)} = \rho_{44}^{(0)} = 0, \quad \text{(B3g)}$$

where $X = 2\,\text{Im}[(d_{42}d_{43} - |\Omega_c|^2)|\Omega_c|^2/Z]$, $Y = -2\,\text{Im}[(d_{42}d_{43} - |\Omega_c|^2 + |\Omega_a|^2)|\Omega_c|^2/Z]$, and $Z = d_{32}d_{42}d_{43} - |\Omega_c|^2 d_{32} - |\Omega_a|^2 d_{43}$.

For the first-order ($m = 1$) approximation, the solution for nonzero matrix elements reads $\rho_{21}^{(1)} = \alpha_{21}^{(1)}\Omega_p$, $\rho_{31}^{(1)} = \alpha_{31}^{(1)}\Omega_p$, and $\rho_{41}^{(1)} = \alpha_{41}^{(1)}\Omega_p$, where $\alpha_{21}^{(1)}$, $\alpha_{31}^{(1)}$, and $\alpha_{41}^{(1)}$ are determined by the equation

$$\begin{pmatrix} d_{21} & \Omega_c^* & 0 \\ \Omega_c & d_{31} & \Omega_a^* \\ 0 & \Omega_a & d_{41} \end{pmatrix}\begin{pmatrix} \alpha_{21}^{(1)} \\ \alpha_{31}^{(1)} \\ \alpha_{41}^{(1)} \end{pmatrix} = \begin{pmatrix} \rho_{23}^{(0)} \\ \rho_{33}^{(0)} - \rho_{11}^{(0)} \\ \rho_{43}^{(0)} \end{pmatrix}. \quad \text{(B4)}$$

The expressions of $\alpha_{21}^{(1)}$, $\alpha_{31}^{(1)}$, and $\alpha_{41}^{(1)}$ are given by

$$\alpha_{21}^{(1)} = \big[(d_{31}d_{41} - |\Omega_a|^2)\rho_{23}^{(0)} + \Omega_c^*\Omega_a^*\rho_{43}^{(0)} - d_{41}\Omega_c^*(\rho_{33}^{(0)} - \rho_{11}^{(0)})\big]/D, \quad \text{(B5a)}$$

$$\alpha_{31}^{(1)} = \big[d_{21}d_{41}(\rho_{33}^{(0)} - \rho_{11}^{(0)}) - d_{41}\Omega_c\rho_{23}^{(0)} - d_{21}\Omega_a^*\rho_{43}^{(0)}\big]/D, \quad \text{(B5b)}$$

$$\alpha_{41}^{(1)} = \big[(d_{21}d_{31} - |\Omega_c|^2)\rho_{43}^{(0)} + \Omega_c\Omega_a\rho_{23}^{(0)} - d_{21}\Omega_a(\rho_{33}^{(0)} - \rho_{11}^{(0)})\big]/D, \quad \text{(B5c)}$$

where $D = d_{21}d_{31}d_{41} - |\Omega_c|^2 d_{41} - |\Omega_a|^2 d_{21}$.

For the second-order ($m = 2$) approximation, the solution for nonzero matrix elements is found to be $\rho_{32}^{(2)} = \alpha_{32}^{(2)}|\Omega_p|^2$, $\rho_{42}^{(2)} = \alpha_{42}^{(2)}|\Omega_p|^2$, $\rho_{43}^{(2)} = \alpha_{43}^{(2)}|\Omega_p|^2$, and $\rho_{jj}^{(2)} = \alpha_{jj}^{(2)}|\Omega_p|^2$, where $\alpha_{32}^{(2)}$, $\alpha_{42}^{(2)}$, and $\alpha_{43}^{(2)}$ satisfy the equation

$$
\begin{pmatrix} d_{32} & \Omega_a^* & 0 \\ \Omega_a & d_{42} & -\Omega_c \\ 0 & -\Omega_c^* & d_{43} \end{pmatrix} \begin{pmatrix} \alpha_{32}^{(2)} \\ \alpha_{42}^{(2)} \\ \alpha_{43}^{(2)} \end{pmatrix}
$$
$$
= \begin{pmatrix} \Omega_c(\alpha_{33}^{(2)} - \alpha_{22}^{(2)}) - \alpha_{12}^{(1)} \\ 0 \\ \Omega_a(\alpha_{44}^{(2)} - \alpha_{33}^{(2)}) + \alpha_{41}^{(1)} \end{pmatrix} \quad \text{(B6)}
$$

and $\alpha_{jj}^{(2)}$ satisfy the equation

$$
\begin{pmatrix} -\Gamma_{21} & 0 & \Gamma_{13} & 0 \\ \Gamma_{21} & 0 & \Gamma_{23} & 0 \\ 0 & 0 & -\Gamma_3 & \Gamma_{34} \\ 1 & 1 & 1 & 1 \end{pmatrix} \begin{pmatrix} \alpha_{11}^{(2)} \\ \alpha_{22}^{(2)} \\ \alpha_{33}^{(2)} \\ \alpha_{44}^{(2)} \end{pmatrix}
$$
$$
= \begin{pmatrix} 2\operatorname{Im}(\alpha_{31}^{(1)}) \\ 2\operatorname{Im}(\Omega_c^*\alpha_{32}^{(2)}) \\ 2\operatorname{Im}(\alpha_{31}^{(1)*} + \Omega_c\alpha_{32}^{(2)*} + \Omega_a^*\alpha_{43}^{(2)}) \\ 0 \end{pmatrix}. \quad \text{(B7)}
$$

However, the expressions for $\alpha_{32}^{(2)}$, $\alpha_{42}^{(2)}$, $\alpha_{43}^{(2)}$, and $\alpha_{jj}^{(2)}$ are too lengthy to be presented here and are treated by numerical means.

The expression of the local Kerr nonlinearity is obtained for the third-order ($m = 3$) approximation, reading $\rho_{21}^{(3)} = \alpha_{21}^{(3)}|\Omega_p|^2\Omega_p$, $\rho_{31}^{(3)} = \alpha_{31}^{(3)}|\Omega_p|^2\Omega_p$, and $\rho_{41}^{(3)} = \alpha_{41}^{(3)}|\Omega_p|^2\Omega_p$. The solutions of $\alpha_{21}^{(3)}$, $\alpha_{31}^{(3)}$, and $\alpha_{41}^{(3)}$ can be obtained from the equation

$$
\begin{pmatrix} d_{21} & \Omega_c^* & 0 \\ \Omega_c & d_{31} & \Omega_a^* \\ 0 & \Omega_a & d_{41} \end{pmatrix} \begin{pmatrix} \alpha_{21}^{(3)} \\ \alpha_{31}^{(3)} \\ \alpha_{41}^{(3)} \end{pmatrix} = \begin{pmatrix} \alpha_{23}^{(2)} \\ \alpha_{33}^{(2)} - \alpha_{11}^{(2)} \\ \alpha_{43}^{(2)} \end{pmatrix}, \quad \text{(B8)}
$$

leading to the expressions

$$
\alpha_{21}^{(3)} = \left[(d_{31}d_{41} - |\Omega_a|^2)\alpha_{23}^{(2)} + \Omega_c^*\Omega_a^*\alpha_{43}^{(2)} \right.
$$
$$
\left. - d_{41}\Omega_c^*(\alpha_{33}^{(2)} - \alpha_{11}^{(2)}) \right]/D, \quad \text{(B9a)}
$$
$$
\alpha_{31}^{(3)} = \left[d_{21}d_{41}(\alpha_{33}^{(2)} - \alpha_{11}^{(2)}) - d_{41}\Omega_c\alpha_{23}^{(2)} \right.
$$
$$
\left. - d_{21}\Omega_a^*\alpha_{43}^{(2)} \right]/D, \quad \text{(B9b)}
$$
$$
\alpha_{41}^{(3)} = \left[(d_{21}d_{31} - |\Omega_c|^2)\alpha_{43}^{(2)} + \Omega_c\Omega_a\alpha_{23}^{(2)} \right.
$$
$$
\left. - d_{21}\Omega_a(\alpha_{33}^{(2)} - \alpha_{11}^{(2)}) \right]/D. \quad \text{(B9c)}
$$

Other density-matrix elements in this order are not needed and hence are omitted here.

[1] Y. S. Kivshar and G. P. Agrawal, *Optical Solitons: From Fibers to Photonic Crystals* (Academic, Cambridge, 2003).

[2] B. A. Malomed, *Multidimensional Solitons* (AIP, Melville, 2022).

[3] Y. V. Kartashov, V. A. Vysloukh, and L. Torner, Soliton shape and mobility control in optical lattices, Prog. Opt. **52**, 63 (2009).

[4] Y. V. Kartashov, B. A. Malomed, and L. Torner, Solitons in nonlinear lattices, Rev. Mod. Phys. **83**, 247 (2011).

[5] V. V. Konotop, J. Yang, and D. A. Zezyulin, Nonlinear waves in $\mathcal{PT}$-symmetric systems, Rev. Mod. Phys. **88**, 035002 (2016).

[6] Y. V. Kartashov, A. A. Egorov, V. A. Vysloukh, and L. Torner, Rotary dipole-mode solitons in Bessel optical lattices, J. Opt. B **6**, 444 (2004).

[7] Y. V. Kartashov, V. A. Vysloukh, and L. Torner, Rotary Solitons in Bessel Optical Lattices, Phys. Rev. Lett. **93**, 093904 (2004).

[8] Y. V. Kartashov, V. A. Vysloukh, and L. Torner, Stable Ring-Profile Vortex Solitons in Bessel Optical Lattices, Phys. Rev. Lett. **94**, 043902 (2005).

[9] Y. V. Kartashov, V. A. Vysloukh, and L. Torner, Soliton spiraling in optically induced rotating Bessel lattices, Opt. Lett. **30**, 637 (2005).

[10] Y. V. Kartashov, R. Carretero-González, B. A. Malomed, V. A. Vysloukh, and L. Torner, Multipole-mode solitons in Bessel optical lattices, Opt. Express **13**, 10703 (2005).

[11] D. Mihalache, D. Mazilu, F. Lederer, B. A. Malomed, Y. V. Kartashov, L.-C. Crasovan, and L. Torner, Stable Spatiotemporal Solitons in Bessel Optical Lattices, Phys. Rev. Lett. **95**, 023902 (2005).

[12] B. B. Baizakov, B. A. Malomed, and M. Salerno, Matter-wave solitons in radially periodic potentials, Phys. Rev. E **74**, 066615 (2006).

[13] F. Ye, Y. V. Kartashov, B. Hu, and L. Torner, Light bullets in Bessel optical lattices with spatially modulated nonlinearity, Opt. Express **17**, 11328 (2009).

[14] L. Dong, J. Wang, H. Wang, and G. Yin, Bessel lattice solitons in competing cubic-quintic nonlinear media, Phys. Rev. A **79**, 013807 (2009).

[15] A. Ruelas, S. Lopez-Aguayo, and J. C. Gutiérrez-Vega, Soliton dynamics in modulated Bessel photonic lattices, Phys. Rev. A **82**, 063808 (2010).

[16] C. Hang and V. V. Konotop, Spatial solitons in a three-level atomic medium supported by a Laguerre-Gaussian control beam, Phys. Rev. A **83**, 053845 (2011).

[17] X. Wang, Z. Chen, and P. G. Kevrekidis, Observation of Discrete Solitons and Soliton Rotation in Optically Induced Periodic Ring Lattices, Phys. Rev. Lett. **96**, 083904 (2006).

[18] S. Huang, P. Zhang, X. Wang, and Z. Chen, Observation of soliton interaction and planetlike orbiting in Bessel-like photonic lattices, Opt. Lett. **35**, 2284 (2010).

[19] N. N. Rosanov, S. V. Fedorov, and A. N. Shatsev, Two-dimensional laser soliton complexes with weak, strong, and mixed coupling, Appl. Phys. B **81**, 937 (2005).

[20] N. A. Veretenov, N. N. Rosanov, and S. V. Fedorov, Motion of complexes of 3D-laser solitons, Opt. Quant. Electron **40**, 253 (2008).

[21] M. Fleischhauer, A. Imamoglu, and J. P. Marangos, Electromagnetically induced transparency: Optics in coherent media, Rev. Mod. Phys. **77**, 633 (2005), and references therein.

[22] Y. Wu and L. Deng, Ultraslow Optical Solitons in a Cold Four-State Medium, Phys. Rev. Lett. **93**, 143904 (2004).

[23] G. Huang, L. Deng, and M. G. Payne, Dynamics of ultraslow optical solitons in a cold three-state atomic system, Phys. Rev. E **72**, 016617 (2005).

[24] S. E. Harris, Refractive-index control with strong fields, Opt. Lett. **19**, 2018 (1994).

[25] C. Hang, V. V. Konotop, and G. Huang, Spatial solitons and instabilities of light beams in a three-level atomic medium with a standing-wave control field, Phys. Rev. A **79**, 033826 (2009).

[26] C. M. Bender and S. Boettcher, Real Spectra in Non-Hermitian Hamiltonians Having $\mathcal{PT}$ Symmetry, Phys. Rev. Lett. **80**, 5243 (1998).

[27] C. M. Bender, Making sense of non-Hermitian Hamiltonians, Rep. Prog. Phys. **70**, 947 (2007).

[28] C. Hang, G. Huang, and V. V. Konotop, $\mathcal{PT}$ Symmetry with a System of Three-Level Atoms, Phys. Rev. Lett. **110**, 083604 (2013).

[29] J. Sheng, M. Miri, D. N. Christodoulides, and M. Xiao, $\mathcal{PT}$-symmetric optical potentials in a coherent atomic medium, Phys. Rev. A **88**, 041803(R) (2013).

[30] Z. Zhang, Y. Zhang, J. Sheng, L. Yang, M. Miri, D. N. Christodoulides, B. He, Y. Zhang, and M. Xiao, Observation of Parity-Time Symmetry in Optically Induced Atomic Lattices, Phys. Rev. Lett. **117**, 123601 (2016).

[31] C. Hang and G. Huang, Parity-time symmetry with coherent atomic gases, Adv. Phys. X **2**, 737 (2017).

[32] Z. Zhang, D. Ma, J. Sheng, Y. Zhang, Y. Zhang, and M. Xiao, Non-Hermitian optics in atomic systems, J. Phys. B **51**, 072001 (2018).

[33] Y. Xue, C. Hang, Y. He, Z. Bai, Y. Jiao, G. Huang, J. Zhao, and S. Jia, Experimental observation of partial parity-time symmetry and its phase transition with a laser-driven cesium atomic gas, Phys. Rev. A **105**, 053516 (2022).

[34] R. El-Ganainy, K. G. Makris, M. Khajavikhan, Z. H. Musslimani, S. Rotter, and D. N. Christodoulides, Non-Hermitian physics and PT symmetry, Nat. Phys. **14**, 11 (2018).

[35] S. V. Suchkov, A. A. Sukhorukov, J. Huang, S. V. Dmitriev, C. Lee, and Y. S. Kivshar, Nonlinear switching and solitons in PT-symmetric photonic systems, Laser Photon. Rev. **10**, 177 (2016).

[36] L. Feng, R. El-Ganainy, and L. Ge, Non-Hermitian photonics based on parity-time symmetry, Nat. Photon. **11**, 752 (2017).

[37] H. Zhao and L. Feng, Parity-time symmetric photonics, Natl. Sci. Rev. **5**, 183 (2018).

[38] Z. H. Musslimani, K. G. Makris, R. El-Ganainy, and D. N. Christodoulides, Optical Solitons in $\mathcal{PT}$-Periodic Potentials, Phys. Rev. Lett. **100**, 030402 (2008).

[39] Z. Shi, X. Jiang, X. Zhu, and H. Li, Bright spatial solitons in defocusing Kerr media with $\mathcal{PT}$-symmetric potentials, Phys. Rev. A **84**, 053855 (2011).

[40] C. Li, C. Huang, H. Liu, and L. Dong, Multipeaked gap solitons in $\mathcal{PT}$-symmetric optical lattices, Opt. Lett. **37**, 4543 (2012).

[41] C. P. Jisha, A. Alberucci, V. A. Brazhnyi, and G. Assanto, Nonlocal gap solitons in $\mathcal{PT}$-symmetric periodic potentials with defocusing nonlinearity, Phys. Rev. A **89**, 013812 (2014).

[42] H. Wang and D. N. Christodoulides, Two dimensional gap solitons in self-defocusing media with PT-symmetric superlattice, Commun. Nonlinear. Sci. Num. Simul. **38**, 130 (2016).

[43] S. Hu, X. Ma, D. Lu, Z. Yang, Y. Zheng, and W. Hu, Solitons supported by complex $\mathcal{PT}$-symmetric Gaussian potentials, Phys. Rev. A **84**, 043818 (2011).

[44] D. A. Zezyulin and V. V. Konotop, Nonlinear modes in the harmonic $\mathcal{PT}$-symmetric potential, Phys. Rev. A **85**, 043840 (2012).

[45] H. Chen, S. Hu, and L. Qi, The optical solitons in the Scarff parity-time symmetric potentials, Opt. Commun. **331**, 139 (2014).

[46] Z. Yan, Z. Wen, and C. Hang, Spatial solitons and stability in self-focusing and defocusing Kerr nonlinear media with generalized parity-time-symmetric Scarff-II potentials, Phys. Rev. E **92**, 022913 (2015).

[47] B. Midya and R. Roychoudhury, Nonlinear localized modes in $\mathcal{PT}$-symmetric Rosen-Morse potential wells, Phys. Rev. A **87**, 045803 (2013).

[48] Y. Eliezer, A. Bahabad, and B. A. Malomed, Superoscillatory $\mathcal{PT}$-symmetric potentials, Phys. Rev. A **98**, 043830 (2018).

[49] S. Hu and W. Hu, Optical solitons in the parity-time-symmetric Bessel complex potential, J. Phys. B **45**, 225401 (2012).

[50] H. Wang, Y. Wei, X. Huang, G. Chen, and H. Ye, Fundamental and dressed annular solitons in saturable nonlinearity with parity-time symmetric Bessel potential, Chin. Phys. B **27**, 044203 (2018).

[51] H. Chen and S. Hu, The solitons in parity-time symmetric mixed Bessel linear potential and modulated nonlinear lattices, Opt. Commun. **332**, 169 (2014).

[52] Here "2D" means the case where the transverse diffraction effect (indicated by the second-order spatial derivatives $\nabla_\perp^2$) plays a role; "3D" means the case where the transverse diffraction effect and longitudinal dispersion effect (indicated by $\nabla_\perp^2$ and $\partial^2/\partial t^2$) play roles.

[53] W. Demtröder, *Laser Spectroscopy: Basic Concepts and Instrumentation*, 3rd ed. (Springer, Berlin, 2003), Chap. 10.

[54] R. W. Boyd, *Nonlinear Optics* (Academic, Amsterdam, 2003).

[55] D. A. Steck, Rubidium 87 D Line Data, http://steck.us/alkalidata.

[56] Q. Zhang, Z. Bai, and G. Huang, Fast-responding property of electromagnetically induced transparency in Rydberg atoms, Phys. Rev. A **97**, 043821 (2018).

[57] J. Arlt and K. Dholakia, Generation of high-order Bessel beams by use of an axicon, Opt. Commun. **177**, 297 (2000).

[58] N. Chattrapiban, E. A. Rogers, D. Cofield, W. T. Hill, and R. Roy, Generation of nondiffracting Bessel beams by use of a spatial light modulator, Opt. Lett. **28**, 2183 (2003).

[59] J. Durnin, J. J. Miceli, Jr., and J. H. Eberly, Diffraction-Free Beams, Phys. Rev. Lett. **58**, 1499 (1987).

[60] K. G. Makris, Z. H. Musslimani, D. N. Christodoulides, and S. Rotter, Constant-intensity waves and their modulation instability in non-Hermitian potentials, Nat. Commun. **6**, 7257 (2015).

[61] Y. Lumer, Y. Plotnik, M. C. Rechtsman, and M. Segev, Nonlinearly Induced $\mathcal{PT}$ Transition in Photonic Systems, Phys. Rev. Lett. **111**, 263901 (2013).

[62] Z. Bai, W. Li, and G. Huang, Stable single light bullets and vortices and their active control in cold Rydberg gases, Optica **6**, 309 (2019).